

# Accurate Lungs Segmentation on CT Chest Images by Adaptive Appearance-Guided Shape Modeling

Ahmed Soliman, *Member, IEEE*, Fahmi Khalifa, *Member, IEEE*, Ahmed Elnakib, *Member, IEEE*, Mohamed Abou El-Ghar, Neal Dunlap, Brian Wang, Georgy Gimel'farb, Robert Keynton, and Ayman El-Baz\*, *Senior Member, IEEE*

**Abstract**—To accurately segment pathological and healthy lungs for reliable computer-aided disease diagnostics, a stack of chest CT scans is modeled as a sample of a spatially inhomogeneous joint 3D Markov-Gibbs random field (MGRF) of voxel-wise lung and chest CT image signals (intensities). The proposed learnable MGRF integrates two visual appearance submodels with an adaptive lung shape submodel. The first-order appearance submodel accounts for both the original CT image and its Gaussian scale space (GSS) filtered version to specify local and global signal properties, respectively. Each empirical marginal probability distribution of signals is closely approximated with a linear combination of discrete Gaussians (LCDG), containing two positive dominant and multiple sign-alternate subordinate DGs. The approximation is separated into two LCDGs to describe individually the lungs and their background, i.e., all other chest tissues. The second-order appearance submodel quantifies conditional pairwise intensity dependencies in the nearest voxel 26-neighborhood in both the original and GSS-filtered images. The shape submodel is built for a set of training data and is adapted during segmentation using both the lung and chest appearances. The accuracy of the proposed segmentation framework is quantitatively assessed using two public databases (ISBI VESSEL12 challenge and MICCAI LOLA11 challenge) and our own database with, respectively, 20, 55, and 30 CT images of various lung pathologies acquired with different scanners and protocols. Quantitative assessment of our framework in terms of Dice similarity coefficients, 95-percentile bidirectional Hausdorff distances, and percentage volume differences confirms the high accuracy of our model on both our database ( $98.4 \pm 1.0\%$ ,  $2.2 \pm 1.0$  mm,  $0.42 \pm 0.10\%$ ) and the VESSEL12 database ( $99.0 \pm 0.5\%$ ,  $2.1 \pm 1.6$  mm,  $0.39 \pm 0.20\%$ ), respectively. Similarly, the accuracy of our approach is further verified via a blind evaluation by the organizers of the LOLA11 competition, where an average overlap of 98.0% with the expert's segmentation is yielded on all 55 subjects with our framework being ranked first among all the state-of-the-art techniques compared.

**Index Terms**—Lung segmentation, computed tomography, adaptive shape model, Markov-Gibbs random field.

## I. INTRODUCTION

**A**utomated lung segmentation on chest CT scans is crucial for efficient computer-aided diagnosis (CAD) of pulmonary diseases, such as, lung cancer. Unfortunately,

Ahmed Soliman, Fahmi Khalifa, Ahmed Elnakib, Robert Keynton, and Ayman El-Baz are with the BioImaging Laboratory, Bioengineering Department, University of Louisville, Louisville, KY 40292, USA.

Neal Dunlap, and Brian Wang are with the Radiation Oncology Department, University of Louisville, Louisville, KY, USA.

Georgy Gimel'farb is with the Department of Computer Science, University of Auckland, Auckland, New Zealand.

Mohamed Abou El-Ghar is with the Radiology Department, Urology and Nephrology Center, University of Mansoura, Mansoura 35516, Egypt.

\* Corresponding author, e-mail: aselba01@louisville.edu.

the large variety of images and diagnostic measurements for different lung pathologies make accurate, fast, and low-cost segmentation a challenge. For instance, pathology-related segmentation failures lose important data, being needed for studying radiation pneumonitis development [1]. As shown by Armato et al. [2] the accuracy of lung segmentation can affect lung nodules detection by 17%.

In the application to CT chest images, most of the earlier segmentation techniques [3]–[9] presume only the lungs are darker than the other chest tissues, which might result in failure to detect nodules in the case of severe lung pathologies. To avoid such failures, more recent lung segmentation methods, which are briefly reviewed below, consider visual appearances [10], [11], shapes [12]–[17], or hybrid techniques [18]–[22] to account for normal and pathological tissues. A more detailed survey of current lung segmentation techniques can be found in [23].

**Appearance-based segmentation** employs texture information to distinguish between objects where the edges are not defined by clear boundaries. Wang et al. [11] used classical Haralick's texture descriptors to discriminate, on chest CT scans, between normal and pathological tissues with unclear boundaries for moderate or severe interstage lung disease (ILD). The descriptors, including energy, entropy, contrast, maximum probability, and inverse difference moment, characterize the local gray-level co-occurrence matrices. First, normal tissues and moderate ILD parenchyma were segmented by simple thresholding of the voxel-wise signals. Then, the abnormal regions with severe ILD, which depict the local descriptors, were found on the appearance images, and combined with the initially segmented regions. This method demonstrated an average overlap of 96.7% with the “gold standard” manual method on a test database of 76 CT scans (31 normal and 45 abnormal lungs). In another study, Korfiatis et al. [18] segmented lung data, including cases with interstitial pneumonia, first by using voxel-wise gray levels only. Subsequently the initial segmentation was refined by classifying the voxels by a support vector machine classifier to account for statistics of both the gray levels and wavelet coefficients, whereas Lassen et al. [19] used a sequence of morphological operations to refine the initial threshold-based segmentation of the pulmonary airspaces. Kockelkorn et al. [21] segmented the lungs with a  $k$ -nearest-neighbor classifier, trained on available prior data; however, to account for severe abnormalities, the user had to interactively correct the initial classification.

**Shape-based segmentation** exploits specific lung shape

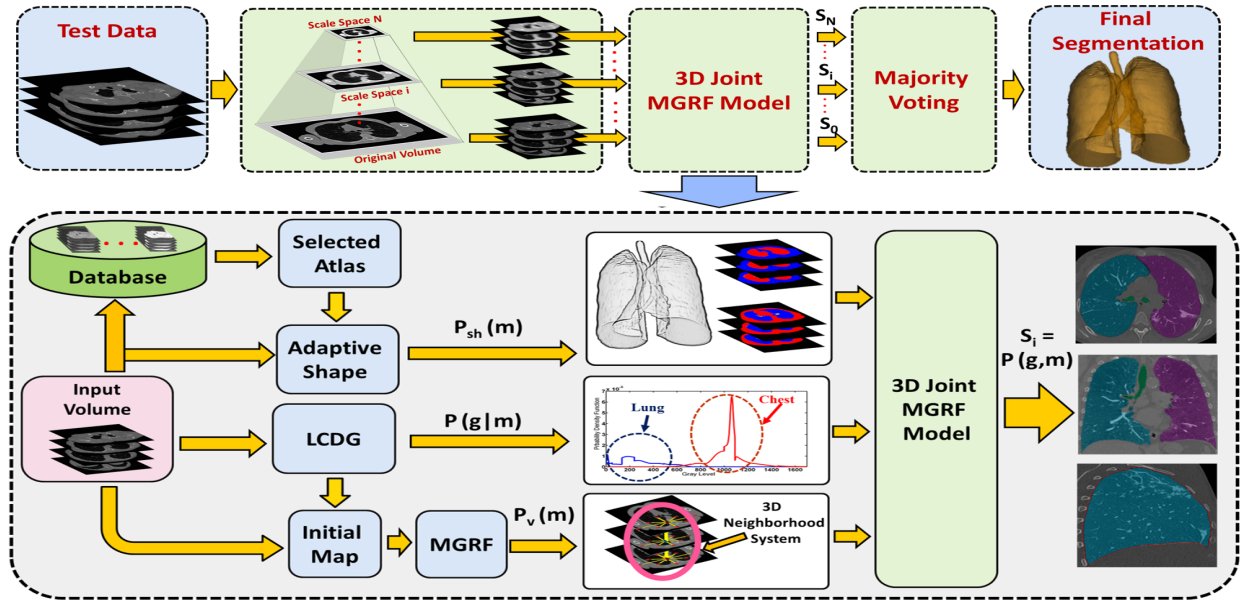


Fig. 1. Our framework for segmenting lungs from chest CT images.

priors with some variability among the scans to yield more accurate segmentation. Sun et al. [15] matched a 3D active shape model to a CT chest scan to roughly define the initial lung borders and then refined the segmented lungs with a global surface optimization method developed by Li et al. [24]. Van Rikxoort et al. [16] segmented the lungs using region growing and morphological operations methods, then automatically performed a multi-atlas-based refinement if a pathology-related segmentation error was detected automatically due to a statistical deviation from a predefined range of lung volume and shape measurements. Sluimer et al. [14] used 15 chest CT scans to build a probabilistic atlas of normal lung fields and registered a pathological lung scan to the atlas in order to segment the lungs with severe pathologies. To segment pathological lungs, Sofka et al. [25] used a set of anatomical landmarks on the ribs and spine to initialize the shape model and then refined the model by iterative surface deformation. Similarly, an atlas-based segmentation model in combination with a deformable model was applied by Zhou et al. [13] to segment lungs with large tumors; whereas, Nakagomi et al. [17] implemented a graph-cut segmentation technique, that incorporated shape and other prior information about neighboring lung structures, on pathological lung images including pleural effusion.

**Hybrid segmentation** combines various segmentation techniques to reach higher accuracies. Birkbeck et al. [20] added statistical learning to anatomical constraints derived from neighboring anatomical structures (heart, liver, spleen, and ribs), to segment lungs. These structures were first detected by statistical classifiers and then used as geometrical constraints for deforming the lung mesh. Mansoor et al. [10] segmented pathological lungs with a wide range of abnormalities in two steps. Initially, the lung parenchyma was segmented on the basis of fuzzy connectedness [26], and the differences between the rib-cage and lung parenchyma volumes were analyzed to determine the pathology. Subsequently, the segmentation

was refined, by applying texture descriptors, to identify the pathological tissues that might have been missed during the initial segmentation procedure. Kockelkorn et al. [12] divided the chest CT scan into 3D volumes-of-interest (VOIs) with voxels of similar intensities and classified each VOI as either the lung or background. Then, the misclassified voxels were corrected either interactively or using a slice-wise supervised classification technique. Hua et al. [22] segmented the lungs by optimizing a graph-supported cost function of voxel-wise intensities and their spatial gradients, taking into account the boundary smoothness and rib constraints.

However, the above methods for automated or semi-automated segmentation of normal and pathological lungs from CT chest images have several drawbacks. Specifically, some of the methods rely on expensive and user-dependent interactions with a radiologist, or depend on anatomical landmarks, which are difficult to determine, especially when pathological tissues are present. Furthermore, when a pathology detector is employed, the overall accuracy considerably decreases after the detection fails. In addition, active appearance models make segmentation too sensitive to model initialization and number of control points. Moreover, most of the methods were designed for a specific type of lung pathology, e.g., nodules, and thus may fail on other types of pathological tissues. To partially overcome these drawbacks, we propose a novel framework, being capable to segment with a high level of accuracy both normal and pathological lungs from chest CT images acquired via various scanners and protocols. Due to integrating an adaptive shape prior with easy-to-learn first-order visual appearance models and a 2<sup>nd</sup>-order 3D MGRF-based model of spatial voxel interactions, the framework is applicable to a wide variety of pathologies, including tumors, pulmonary sarcoidosis, pleural effusion, consolidation, fibrosis, and cavities. To the best of our knowledge, we are the first to introduce a probabilistic map accounting for not only region labels, but also intensities in neighboring spatial voxel

161 locations as an adaptive shape prior. The framework, detailed  
 162 in Section II, was extensively validated on three databases  
 163 (Section III) and ranked first by the third-party evaluation of  
 164 LOLA11 challenge.

## 165 II. METHODS

166 All 3D CT chest scans are initially pre-processed to identify  
 167 their background voxels, (air and bed), by region growing  
 168 and analyzing connected components. Because detailed prior  
 169 information about lung shapes significantly improves the seg-  
 170 mentation accuracy, our framework (Fig. 1) builds a spatially-  
 171 variant shape prior from a pre-selected training database of  
 172 3D CT scans of normal and pathological lungs. The train-  
 173 ing scans are accurately co-aligned using a B-spline-based  
 174 nonrigid registration [27], detailed in Section II-A. Unlike  
 175 more conventional alternatives, the proposed shape prior is  
 176 adapted to a given input, or test CT scan. The latter is similarly  
 177 aligned to the training database and a 3D deformation field of  
 178 aligning voxel-to-voxel translations is stored in order to guide  
 179 the process of building the shape prior.

180 The framework analyzes both the original input and its  
 181 Gaussian scale-space (GSS) versions, being formed by con-  
 182 volving with 3D moving Gaussian kernels [28] (Section II-B).  
 183 The GSS smoothing adds longer-range properties to original  
 184 voxel-wise intensities and their pairwise co-occurrences in the  
 185 nearest 26-neighborhoods of each voxel. For segmenting the  
 186 input image, first- and second-order lungs-background models  
 187 are learned and combined with the shape priors separately for  
 188 the input image and each of its GSS versions. The first-order  
 189 models are built by accurate LCDG-based approximations  
 190 of empirical marginal probability distributions of intensities  
 191 over the whole image and estimations of individual marginal  
 192 distributions of the lung and background intensities [29] (Sec-  
 193 tion II-C). The 2<sup>nd</sup>-order spatially uniform MGRF models with  
 194 multiple pairwise interactions of the nearest-neighbor region  
 195 labels [30] are learned to describe initial lungs-background  
 196 region maps (Section II-D).

197 The input image, as well as each of its smoothed GSS  
 198 versions, is separately segmented by combining their learned  
 199 probabilistic first- and 2<sup>nd</sup>-order models together with the  
 200 adaptive shape priors into a joint MGRF model of images  
 201 and their region maps (Section II-E). Finally, a majority rule  
 202 is used to merge the resulting separate segmentations into a  
 203 final lung-background region map (Section II-F).

204 *Basic notation:* Let  $\mathbf{Q} = \{0, 1, \dots, Q - 1\}$  and  $\mathbf{K} =$   
 205  $\{0, 1\}$  be a finite set of integer gray levels and region labels  
 206 (background chest tissues – “0”, and lung tissues – “1”),  
 207 respectively. Let  $\mathbf{r} = (x, y, z)$  be a voxel in integer 3D  
 208  $(x, y, z)$ -coordinates spanning from  $(0, 0, 0)$  to  $(X, Y, Z)$ . Let  
 209 a finite 3D arithmetic lattice  $\mathbf{R} = \{\mathbf{r} = (x, y, z) : 0 \leq x \leq$   
 210  $X, 0 \leq y \leq Y, 0 \leq z \leq Z\}$  support the grayscale CT images,  
 211  $\mathbf{g} = \{g_{\mathbf{r}} : \mathbf{r} \in \mathbf{R}; g_{\mathbf{r}} \in \mathbf{Q}\}$ , and their region, or segmentation  
 212 maps,  $\mathbf{m} = \{m_{\mathbf{r}} : \mathbf{r} \in \mathbf{R}; m_{\mathbf{r}} \in \mathbf{K}\}$ .

### 213 A. Adaptive probabilistic shape prior

214 The proposed appearance-guided adaptive shape prior is  
 215 built from a pre-selected and manually segmented training  
 216 database of 3D chest CT scans.

217 To reduce variations and maximize overlaps between the  
 218 lungs for estimating the prior, each source volume  $f$  (i.e.,  
 219 each of the database subjects) is aligned to the target volume,  
 220 or reference template  $g$  on a domain  $\Omega \subset \mathbb{R}^3$  by using a non-  
 221 rigid registration. Given a certain source  $f$ , the registration  
 222 estimates the deformation field  $\mathcal{T}$  for all  $x \in \Omega$ , by displacing  
 223 a sparse grid,  $\Omega' \subset \Omega$ ; ( $|\Omega'| \ll |\Omega|$ ), of control points,  $\xi$ :

$$\mathcal{T}(x) = x + \sum_{\xi \in \Omega'} \zeta(\|x - \xi\|) \Delta_{\xi} \quad (1)$$

224 where  $\Delta_{\xi}$  is the displacement vector of the control point  $\xi$  and  
 225 the weighting function  $\zeta(\cdot)$  measures the contribution of any  
 226 control point in  $\Omega'$  to the displacement of a point in  $\Omega$ . The  
 227 goal deformation field minimizes the point-wise dissimilarity  
 228 between the target  $g$  and the deformed source  $f$ :

$$E(\mathcal{T}) = \frac{1}{|\Omega'|} \sum_{\xi \in \Omega'} \int \frac{\phi(g(x), f(\mathcal{T}(x)))}{\zeta(\|x - \xi\|)} dx \quad (2)$$

229 where  $\phi$  is the dissimilarity function (we used the sum of  
 230 absolute differences). The objective function in Eq. (2) is mini-  
 231 mized using a Markov random field model of displacements of  
 232 the control points  $\xi$  [31]. The dense displacement field is then  
 233 determined from the control point displacements through rep-  
 234 resenting free form deformations (FFDs) via cubic B-splines.  
 235 We have selected this method because it is fully automated  
 236 (no manual initialization or hand-picked landmarks) and has  
 237 low computational time. More details can be found in [27],  
 238 [31], [32].

239 To handle both the normal and pathological lungs, our  
 240 database,  $\mathbf{S} = \{\mathbf{s}_i = (\mathbf{g}_i, \mathbf{m}_i) : i = 1, 2, \dots, N\}$ , contains 3D  
 241 scans of different normal and pathological lungs, having been  
 242 chosen to represent typical inter-subject variations, and their  
 243 true region maps. The database subjects are selected using  
 244 the principal component analysis (PCA). The PCA calculates  
 245 principal components (PCs) of the covariance matrix between  
 246 all the available subjects from the database (50 subjects in  
 247 our work). Then, instead of defining a new template domain  
 248 for the top  $N$  PCs, the original  $N$  subjects with the highest-  
 249 magnitude coefficients of each of the top  $N$  PCs are selected  
 250 to approximate projections computed by the PCA [33] for  
 251 each test image. In our experiments below, the  $N = 20$  train-  
 252 ing images, having been selected from our locally acquired  
 253 database of 50 subjects, had different sizes, data spacing,  
 254 and slice thickness, which ranged from  $512 \times 512 \times 270$  to  
 255  $512 \times 512 \times 450$ ; 0.703 to 1.37 mm, and 0.703 to 2.50  
 256 mm, respectively. Co-aligning these images with the reference  
 257 template overcomes their variations and makes their size and  
 258 resolution identical. Because every training image has its  
 259 own deformation field that maps its voxels to the reference  
 260 template, accurate mappings between the template and training  
 261 images are guaranteed.

262 A test 3D CT image  $t$  to be segmented is co-aligned  
 263 with the training database using the same template and B-  
 264 spline-based nonrigid registration [27]. Then its customized  
 265 atlas is extracted by computing conventional normalized cross  
 266 correlations (NCC) of Eq. (3) between the chest region in the  
 267 aligned test image  $t$  and the chest region in each database

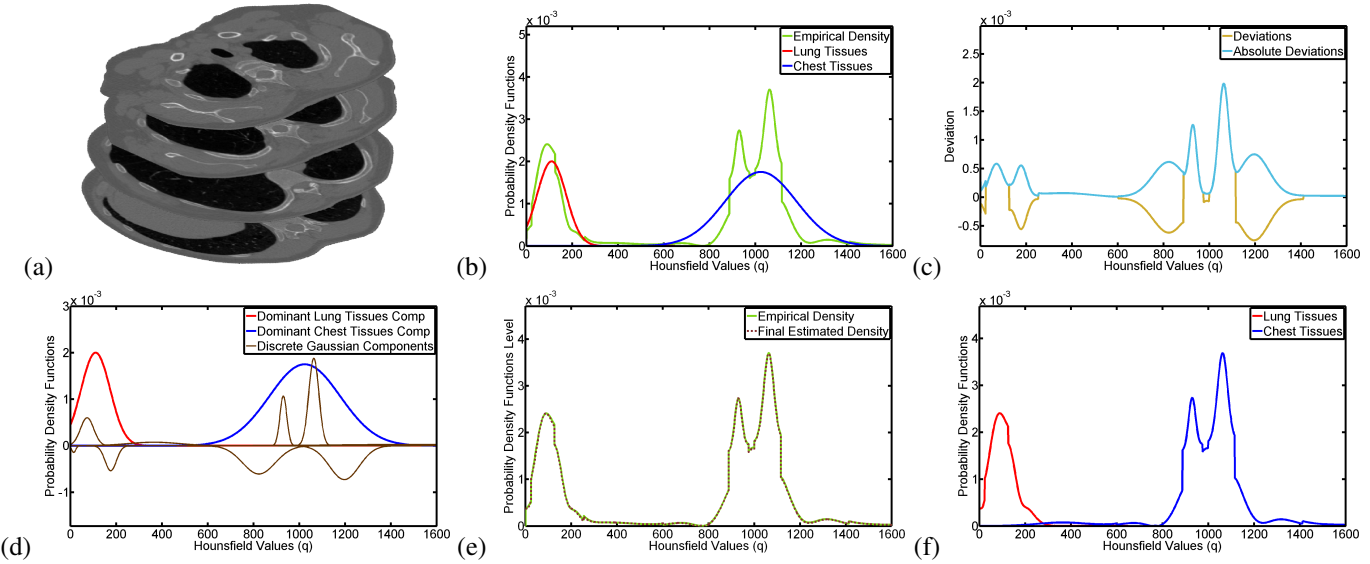


Fig. 2. Typical 3D CT data (a) and its marginal intensity approximated using only two dominant DGs (b); the deviation between the empirical and estimated marginals (c); the dominant and subordinate DGs (d); the final estimated LCDG (e), and the final conditional LCDG models of lung and chest intensities (f).

268 image,  $\mathbf{g}_{l:i}$ , to select the top  $J$  similar lungs.

$$NCC_{\mathbf{t}, \mathbf{g}_i} = \frac{\sum_{\mathbf{r} \in \mathbf{R}} (\mathbf{t}_{\mathbf{r}} - \mu_{\mathbf{t}})(\mathbf{g}_{i:\mathbf{r}} - \mu_{\mathbf{g}_{l:i}})}{\sqrt{\sum_{\mathbf{r} \in \mathbf{R}} (\mathbf{t}_{\mathbf{r}} - \mu_{\mathbf{t}})^2} \sqrt{\sum_{\mathbf{r} \in \mathbf{R}} (\mathbf{g}_{i:\mathbf{r}} - \mu_{\mathbf{g}_i})^2}} \quad (3)$$

269 where  $\mu_{\mathbf{t}}$  and  $\mu_{\mathbf{g}_i}$  are the average intensities for  $\mathbf{t}$  and  $\mathbf{g}_i$ .

270 Visual appearances of the test and training images guide  
271 the shape prior adaptation as follows (this process is also out-  
272 lined in Algorithm 1 summarizing the proposed segmentation  
273 framework). Each voxel  $\mathbf{r}$  of the test image  $\mathbf{t}$  is mapped to  
274 the database lattice by the deformation field aligning  $\mathbf{t}$  to  
275 the database. A subject-specific atlas is built from the top  
276  $J$ ;  $J \leq N$ , training images  $\mathbf{g}_i$  selected in accord with their  
277 correlations  $NCC_{\mathbf{t}, \mathbf{g}_i}$  of Eq. (3) ( $J = 15$  in our experiments  
278 below). To adapt the shape prior at each mapped location  $\mathbf{r}$ , an  
279 initial search cube  $\mathbf{C}_{\mathbf{r}}$  of size  $n_{x:i} \times n_{y:i} \times n_{z:i}$  is centered at the  
280 mapped location  $\mathbf{r}$  for finding in the cube all the atlas voxels  
281 with signal deviations to within a predefined fixed range,  $\tau$ ,  
282 from the mapped input signal,  $t_{\mathbf{r}}$ . If such voxels are absent  
283 in the atlas, the cube size increases iteratively until the voxels  
284 within the predefined signal deviation range are found or the  
285 final cube size is reached ( $n_{x:i} = n_{y:i} = n_{z:i} = 3$ ;  $\tau$  from 50 to  
286 125 with the step of  $\Delta_{\tau} = 25$ , and the final cube size of  $n_{x:f} =$   
287  $n_{y:f} = n_{z:f} = 11$  were used in our experiments below). Then  
288 the voxel-wise probabilities,  $P_{sh:\mathbf{r}}(k)$ ;  $k \in \mathbf{K}$ , for the adaptive  
289 shape prior  $P_{sh}(\mathbf{m}) = \prod_{\mathbf{r} \in \mathbf{R}} P_{sh:\mathbf{r}}(m_{\mathbf{r}})$  are estimated based  
290 on the found voxels of similar appearance and their region  
291 labels. Let  $\nu_{j:\mathbf{r}} = \{\rho : \rho \in \mathbf{R}; \rho \in \mathbf{C}_{\mathbf{r}}; |g_{j:\rho} - t_{\mathbf{r}}| \leq \tau\}$  be  
292 a subset of similar training voxels within the cube  $\mathbf{C}_{\mathbf{r}}$  in the  
293 training image  $\mathbf{g}_j$ . Let  $\nu_{j:\mathbf{r}} = \text{card}(\nu_{j:\mathbf{r}})$  denote the cardinality  
294 (number of voxels) of this subset;  $\nu_{\mathbf{r}} = \sum_{j=1}^J \nu_{j:\mathbf{r}}$ , and  $\delta(z)$   
295 be the Kronecker's delta-function:  $\delta(0) = 1$  and 0 otherwise.  
296 Then

$$P_{sh:\mathbf{r}}(k) = \frac{1}{\nu_{\mathbf{r}}} \sum_{j=1}^J \sum_{\rho \in \nu_{j:\mathbf{r}}} \delta(k - m_{j:\rho}) \quad (4)$$

### B. Gaussian scale space (GSS) smoothing

298 This operation  $\mathbf{g}_{\sigma} = \mathbf{g} * \mathbf{h}_{\sigma}$  convolves a 3D CT image  $\mathbf{g}$  with  
299 a 3D Gaussian kernel  $\mathbf{h}_{\sigma:\mathbf{r}-\mathbf{c}} = (h_{\sigma:\mathbf{r}-\mathbf{c}} : (\mathbf{r}, \mathbf{c}) \in \mathbf{R}^3)$  [28]:  
300

$$h_{\sigma:\mathbf{r}-\mathbf{c}} = \frac{1}{(2\pi)^{1.5}\sigma^3} \exp\left(-\frac{1}{2\sigma^2}|\mathbf{r} - \mathbf{c}|^2\right) \quad (5)$$

301 where  $|\mathbf{r} - \mathbf{c}| = \sqrt{(x - x_c)^2 + (y - y_c)^2 + (z - z_c)^2}$  denotes  
302 the Cartesian voxel-to-voxel distance and  $\mathbf{c} = (x_c, y_c, z_c)$   
303 is the kernel's center. The GSS smoothing reduces signal  
304 noise affecting some chest CT scans, integrates longer-range  
305 properties of the scans in each voxel-wise signal, and excludes  
306 some distortions that may be caused by pathologies. Because  
307 it flattens the original image, i.e., decreases the maximal and  
308 increases the minimal intensities, only two versions smoothed  
309 with the kernels  $9 \times 9 \times 5$ ;  $\sigma^2 = 4.5$ , and  $17 \times 17 \times 5$ ;  
310  $\sigma^2 = 8.5$ ; were used in our experiments below to extend the  
311 overall description of the CT image without losing too many  
312 details and affecting the segmentation accuracy.

### C. First-order appearance (intensity) modeling

313 To accurately separate and approximate conditional  
314 marginal probability distributions of intensities (Hounsfield  
315 units) for the lungs and surrounding chest tissues, the CT  
316 image is modeled as a simple independent random field (IRF)  
317 with the same mixed distribution of intensities at each voxel.  
318 The mixed empirical distribution of the voxel-wise intensities  
319 over the whole image is approximated with an LCDG with two  
320 dominant positive DGs and multiple sign-alternate (positive  
321 and negative) subordinate DGs. The number of the subordinate  
322 DGs and parameters (means and variances) of all the DGs are  
323 estimated with the classical Expectation-Maximization (EM)  
324 algorithm and its modification accounting for the alternate  
325 signs of the DGs [34]. Then the obtained LCDG is separated  
326

---

**Algorithm 1** Proposed lung segmentation framework.

---

- **Input:** Read a given test 3D CT image and form its smoothed GSS versions.
  - **Appearance-guided estimation of the adaptive shape priors:**
    1. Align the test image to the training database and obtain its voxel-wise deformation field.
    2. Construct the subject-specific atlas of the  $J$  top training images by their cross-correlation with the test image.
    3. Estimate the appearance-guided adaptive shape prior  $P_{sh}(\mathbf{m})$  separately for the original and GSS-smoothed test images by calculating the voxel-wise empirical probabilities of the relevant training lungs-background labels:
      - (a) Map each test voxel to the atlas lattice using the found deformation field.
      - (b) Center the initial  $n_{x,i} \times n_{y,i} \times n_{z,i}$  search cube at the mapped voxel.
      - (c) Find within the search cube all the atlas voxels, being close to the test voxel-wise intensity (Hounsfield value) to within a predefined range of  $\pm\tau$ .
      - (d) If no such voxels are found, increase the search cube iteratively and repeat Steps 3.(b)–(c) until the relevant voxels are found or a predefined maximum cube size is reached.
      - (e) If no such voxels are found, increase iteratively the tolerance  $\tau$  by  $\Delta\tau$  and repeat Steps 3.(b)–(d) until such voxels are found.
      - (f) Compute the empirical voxel-wise label probabilities based on relative occurrences of each label over all the found relevant voxels.
  - Segment the lungs individually on the original and GSS-smoothed images:
    - 1) Find an initial region map  $\mathbf{m}$  by the voxel-wise Bayesian maximum a posteriori classification of the test image using its estimated shape prior.
    - 2) Identify the conditional appearance (intensity) model  $P(\mathbf{g}|\mathbf{m})$  by approximating with the LCDGs, the marginal probability distributions of signals associated with one of the two dominant modes of the mixed empirical marginal for the whole test image.
    - 3) Use the initial region map,  $\mathbf{m}$ , to identify the second-order MGRF model,  $P_V(\mathbf{m})$ , of spatially invariant maps.
    - 4) Perform the final Bayesian segmentation of the lungs using the joint MGRF model of Eq. (10).
  - **Output:** The final lungs segmentation by combining individually segmented original and GSS-smoothed images with the majority voting.
- 

327 into conditional lung and chest intensity models for defining  
328 the conditional IRF of image signals, given a region map:

$$P(\mathbf{g}|\mathbf{m}) = \prod_{\mathbf{r} \in \mathbf{R}} p_{m_r}(g_r) \quad (6)$$

329 Basic steps of estimating the conditional lung and chest LCDG  
330 models,  $P_k = (p_k(q) : q \in \mathbf{Q})$ ;  $k \in \mathbf{K} = \{0, 1\}$ , are  
331 illustrated in Fig. 2, and Fig. 3 shows a 3D CT image; its  
332 GSS-version for the  $33 \times 33 \times 5$  kernel, and the corresponding  
333 final estimated conditional LCDG models for chest and lung  
334 marginals.

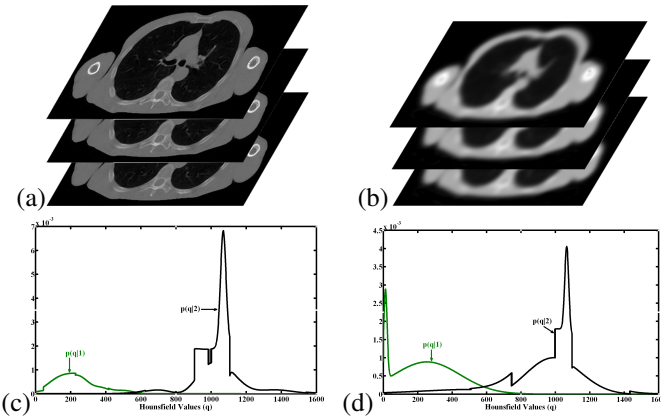


Fig. 3. 3D CT image (a) and its GSS-filtered version (b) for the  $33 \times 33 \times 5$  kernel, with the final estimated conditional LCDG models for chest and lung marginals (c,d).

335 **D. Modeling pairwise spatial interactions of lung labels**

336 To account for lungs inhomogeneities that may affect  
337 the initial Bayesian segmentation, spatial dependencies be-  
338 tween the lung voxels are modeled with a spatially invariant

second-order MGRF [29], [30] with the nearest voxel 26-neighborhood. This modeling enhances the initial segmentation by calculating the likelihood of each voxel to be lung or non-lung on the basis of the initial labeling of the adjacent voxels. By symmetry considerations, the dependencies are uniform, i.e., independent of orientations in the lattice. Let  $\mathbf{V}_a = \{V_a(k, k') = V_{a,eq} \text{ if } k = k' \text{ and } V_a(k, k') = V_{a,ne} \text{ if } k \neq k' : k, k' \in \mathbf{K}\}$  denote bi-valued Gibbs potentials describing three types of symmetric pairwise dependencies between the labels:  $a \in \mathbf{A} = \{\text{hvdc}, \text{hvdu}, \text{hvdl}\}$  where hvdc, hvdu, and hvdl indicate the horizontal-vertical-diagonal dependencies between each voxel and its closest 26-neighbors in the current (c), upper (u), and lower (l) CT slices, respectively, specified by the subsets of inter-voxel coordinate offsets:  $\mathbf{N}_{\text{hvdc}} = \{(\pm 1, 0, 0), (0, \pm 1, 0)\}$ ,  $\mathbf{N}_{\text{hvdu}} = \{(0, 0, 1), (\pm 1, \pm 1, 1)\}$ , and  $\mathbf{N}_{\text{hvdl}} = \{(0, 0, -1), (\pm 1, \pm 1, -1)\}$ . Then the Gibbs probability distribution of region maps is proportional to:

$$P_V(\mathbf{m}) \propto \exp \left( \sum_{\mathbf{r} \in \mathbf{R}} \sum_{a \in \mathbf{A}} \sum_{\boldsymbol{\nu} \in \mathbf{N}_a} V_a(m_{\mathbf{r}}, m_{\mathbf{r}+\boldsymbol{\nu}}) \right) \quad (7)$$

This MGRF is identified by using the approximate analytical maximum likelihood estimates of the potentials [29], [30]:

$$V_{a,eq} = \frac{K^2}{K-1} (f_{eq:a}(\mathbf{m}) - \frac{1}{K}) = 4f_{eq:a}(\mathbf{m}) - 2 \quad (8)$$

$$V_{a,ne} = \frac{K^2}{K-1} (f_{ne:a}(\mathbf{m}) - 1 + \frac{1}{K}) = 4f_{ne:a}(\mathbf{m}) - 2$$

where  $f_{eq:a}(\mathbf{m})$  and  $f_{ne:a}(\mathbf{m})$  are empirical probabilities of the equal and non-equal labels pairs, respectively, in all the equivalent voxel pairs  $\{(\mathbf{r}, \mathbf{r} + \boldsymbol{\nu}) : \boldsymbol{\nu} \in \mathbf{N}_a, \mathbf{r} \in \mathbf{R}\}$ .

361 **E. Joint MGRF model of 3D chest CT images**

To initially segment the lungs, the above unconditional adaptive shape prior,  $P_{sh}(\mathbf{m})$ , conditional first-order appearance model,  $P(\mathbf{g}|\mathbf{m})$ , and unconditional second-order model,

365  $P_V(\mathbf{m})$  of spatial dependencies between the lung labels in  
 366 Eqs. (7) and (8) are integrated into a joint MGRF model of  
 367 either original, or GSS-smoothed images,  $\mathbf{g}$ , and their region  
 368 maps,  $\mathbf{m}$ :

$$P(\mathbf{g}, \mathbf{m}) = P(\mathbf{g}|\mathbf{m}) \underbrace{P_{sh}(\mathbf{m}) P_V(\mathbf{m})}_{P(\mathbf{m})} \quad (9)$$

369 Both the images and region maps are co-aligned to the subject-  
 370 specific atlas defining the shape prior. The Bayesian maximum  
 371 a posteriori estimate,  $\mathbf{m}^* = \arg \max_{\mathbf{m}} L(\mathbf{g}, \mathbf{m})$ , of the region  
 372 map, given an image  $\mathbf{g}$ , maximizes the log-likelihood

$$L(\mathbf{g}, \mathbf{m}) = \log P(\mathbf{g}|\mathbf{m}) + \log P_{sh}(\mathbf{m}) + \log P_V(\mathbf{m}) \quad (10)$$

### 373 F. Classification using majority voting

374 The majority voting, which is popular in fusing concurrent  
 375 decisions, is a special case of the weighted voting. Our final  
 376 segmentation map,  $\hat{\mathbf{m}}$ , combines by the majority voting the  
 377 individual Bayesian region maps  $\mathbf{m}$  and  $\mathbf{m}_l$ , having been built  
 378 separately for the original image,  $\mathbf{t}$ , and its  $L$  GSS-transformed  
 379 versions,  $\mathbf{t}_{l:\sigma_l}; l = 1, \dots, L$ :

$$\hat{\mathbf{m}}_r = \arg \max_{k \in \{0,1\}} \left\{ \delta(k - m_r) + \sum_{l=1}^L \delta(k - m_{l:r}) \right\} \quad (11)$$

380 The two GSS kernels:  $l = 1, 9 \times 9 \times 5; \sigma_1^2 = 4.5$ , and  $l = 2,$   
 381  $17 \times 17 \times 5, \sigma_2^2 = 8.5$  – were used in our experiments below.

382 The main algorithmic components of our framework are  
 383 detailed in Appendix A and Figs. 14– 17.

## 384 III. EXPERIMENTAL RESULTS

385 The segmentation accuracy and robustness were evaluated  
 386 on our own collection of 3D CT chest images for 30 subjects,  
 387 abbreviated UoLDB below, and two publicly available  
 388 sets from the ISBI 2012 VESSEL SEgmentation in the Lung  
 389 (VESSEL) challenge [35], [36] (20 subjects) and MICCAI  
 390 2011 LObe and Lung Analysis (LOLA11) challenge [37]  
 391 (55 subjects). The images have been acquired with different  
 392 scanners and data collection protocols and presented both  
 393 normal lungs and various lung pathologies.

394 The 50 (20 training and 30 test) UoLDB images of size  
 395 from  $512 \times 512 \times 270$  to  $512 \times 512 \times 450$  have been collected  
 396 with a multi-detector GE Light Speed Plus scanner (General  
 397 Electric, Milwaukee, USA) with the imaging protocols of  
 398 140 kV; 100 mA; slice thickness from 0.703 to 2.50 mm;  
 399 scanning pitch 1.5, and field-of-view 36 cm. Figure 4 details  
 400 our 3D lung segmentation results for one subject from the  
 401 UoLDB. Our segmentation employs only two GSS filtering  
 402 stages because its overall accuracy improved insignificantly  
 403 beyond the second stage in a few pilot experiments.

404 In order to highlight advantages of the integration of visual  
 405 appearance descriptors with the adaptive shape descriptor, the  
 406 test UoLDB images were also segmented by combining only  
 407 the visual appearance descriptors, characterizing the original  
 408 and GSS-filtered intensities and their pairwise co-occurrences.  
 409 The resulting accuracy for three UoLDB subjects in Fig. 15  
 410 was low – due to similar original voxel intensities, the patho-  
 411 logical lung tissues were included into the segmented chest,

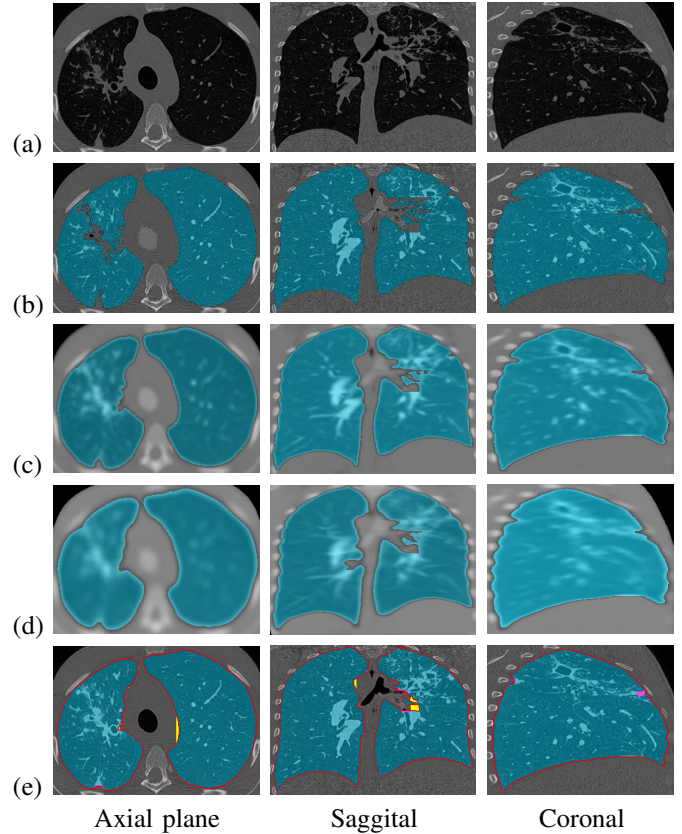


Fig. 4. 3D lung segmentation (the UoLDB): 2D cross-sections of an original image (a); its segmentation (b); segmentation of the GSS-filtered images with  $9 \times 9 \times 5$  (c) and  $17 \times 17 \times 5$  (d) kernels, and final segmentation (e) with color-coded ground truth edges, false positive errors, and false negative errors (red, yellow, and pink points, respectively). Only these two kernels were used in our experiments, because after the second smoothing the overall segmentation accuracy improves insignificantly.

412 rather than lungs. The segmentation error decreased after  
 413 adding the GSS-filtered appearance descriptors and improved  
 414 even further after integrating all the appearance descriptors  
 415 with the adaptive shape prior. More results for subjects with  
 416 different types of pathologies are shown in Fig. 6.

TABLE I  
 DSC, BHD, AND PVD ACCURACY (MEAN  $\pm$  STANDARD DEVIATION) OF  
 DIFFERENT COMPONENTS (FEATURE GROUPS FG) OF OUR FRAMEWORK  
 ON THE UoLDB IN TERMS OF THE : FG1(INTENSITIES AND SPATIAL  
 INTERACTIONS), FG2 (COMBINED ORIGINAL / GSS-FILTERED  
 INTENSITIES AND SPATIAL INTERACTIONS), FG3 (FG2 + ADAPTIVE  
 SHAPE PRIORS).

UoLDB (30 test images)			
	DSC, %	BHD, mm	PVD,
FG1	$0.932 \pm 0.032$	$13.2 \pm 4.6$	$9.90 \pm 7.20$
FG2	$0.966 \pm 0.017$	$9.53 \pm 2.92$	$2.90 \pm 0.70$
FG3	$0.984 \pm 0.010$	$2.20 \pm 1.00$	$0.42 \pm 0.10$
p-value	$< 0.0001$	$< 0.0001$	$< 0.0001$

417 The segmentation accuracy was evaluated for each test 3D  
 418 CT image with the Dice similarity coefficient (DSC) [38], bidi-  
 419 rectional Hausdorff distance (BHD), and percentage volume  
 420 difference (PVD) [39], which characterize spatial overlaps,

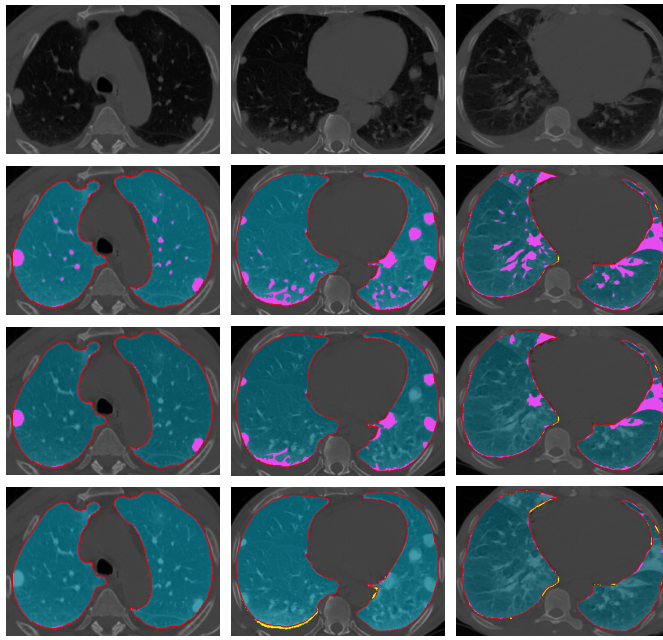


Fig. 5. Impacts of elements of our segmentation for 3 UoLDB subjects: original 2D chest sections (*first row*) and lung regions found for the original intensities and spatial interactions (*second row*); combined original/GSS-filtered intensities and spatial interactions (*third row*); and combined original/GSS-filtered intensities and spatial interactions, together with the adaptive shape model (*fourth row*). Same color ground truth and error coding as in Fig. 4.

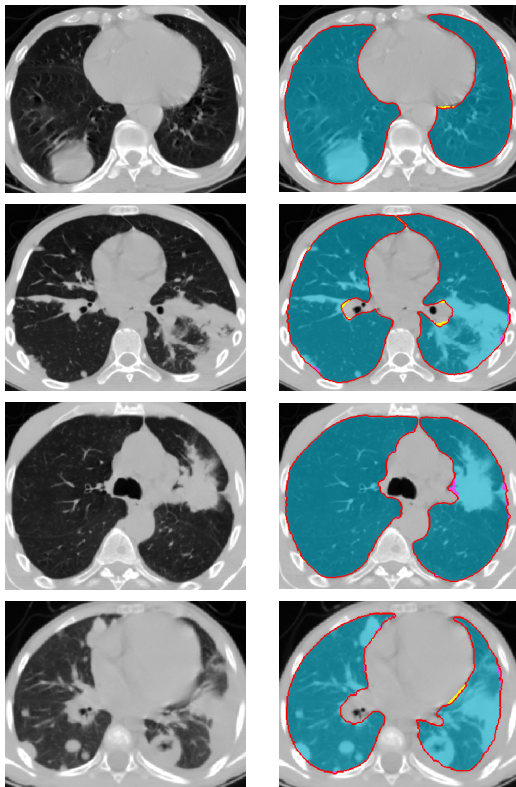


Fig. 6. Other 4 subjects from the UoLDB: original CT chest images with different pathologies: (left: *from top to bottom*) lung mass; consolidation; lung cancer, and cavitation + consolidation pathologies, and our segmentation (right: the same color ground truth and error coding as in Fig. 4).

TABLE II  
DSC, BHD, AND PVD ACCURACY (MEAN $\pm$ STANDARD DEVIATION) OF OUR AND FC SEGMENTATION [10] ON THE UoLDB AND VESSEL [35] DATABASES.

	UoLDB (30 test images)		
	DSC, %	BHD, mm	PVD,
Our segm.	0.984 $\pm$ 0.010	2.20 $\pm$ 1.00	0.42 $\pm$ 0.10
FC [10]	0.906 $\pm$ 0.098	19.0 $\pm$ 9.9	15.4 $\pm$ 15.3
<i>p</i> -value	< 0.0001	< 0.0001	< 0.0001
	VESSEL [35] (20 test images)		
Our segm.	0.990 $\pm$ 0.005	2.10 $\pm$ 1.60	0.39 $\pm$ 0.20
FC [10]	0.967 $\pm$ 0.013	11.5 $\pm$ 5.1	2.40 $\pm$ 1.20
<i>p</i> -value	< 0.0001	< 0.0001	< 0.0001

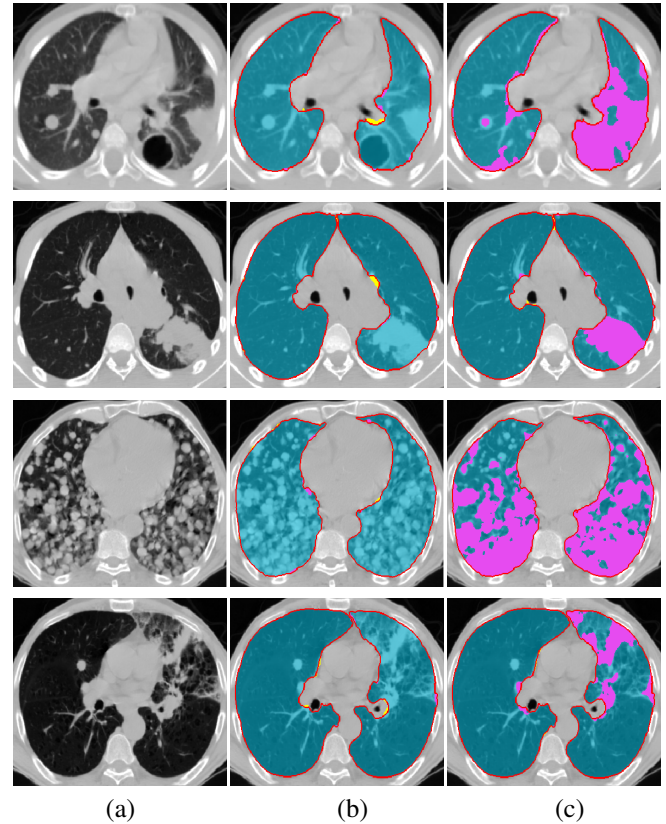


Fig. 7. Comparative segmentation of the UoLDB: (a) original CT sections with, *from top to bottom*, plural effusion and lung nodules; consolidation; pulmonary sarcoidosis, and fibrosis; (b) our segmentation, and (c) the FC segmentation [10] (the same color ground truth and error coding as in Fig. 4).

maximum surface-to-surface distances, and volume differences, respectively, between the segmented and “ground-truth” lung regions. Table I summarizes the DSC, BHD, and PVD statistics for all the test UoLDB data to show the effect of different feature groups (FG) of our framework. The ground-truth lung borders were outlined manually by a radiologist.

The accuracy of our pathological lungs segmentation method is also highlighted by comparing its performance against the traditional fuzzy connectedness (FC)-based lung segmentation [10], having a publicly available open-source software Lung Segmentation Tool (<http://www.nitrc.org/projects/nihlungseg/>). These experiments used the best per-

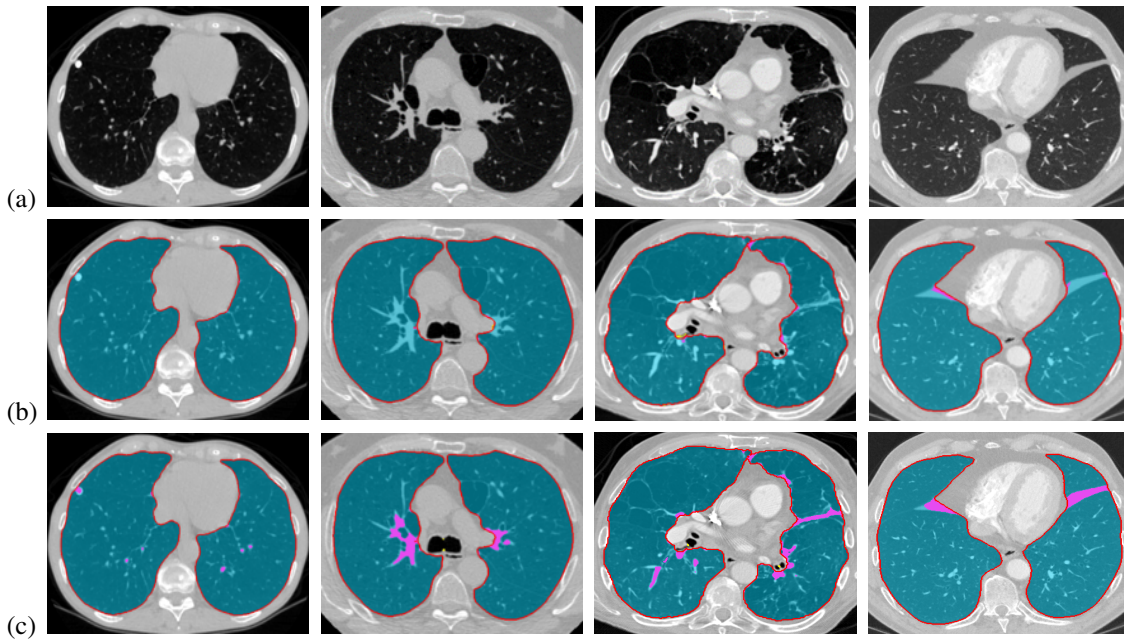


Fig. 8. Comparative segmentation of the VESSEL [35] database: (a) original CT sections; (b) our segmentation, and (c) the FC segmentation [10] (the same color ground truth and error coding as in Fig. 4).

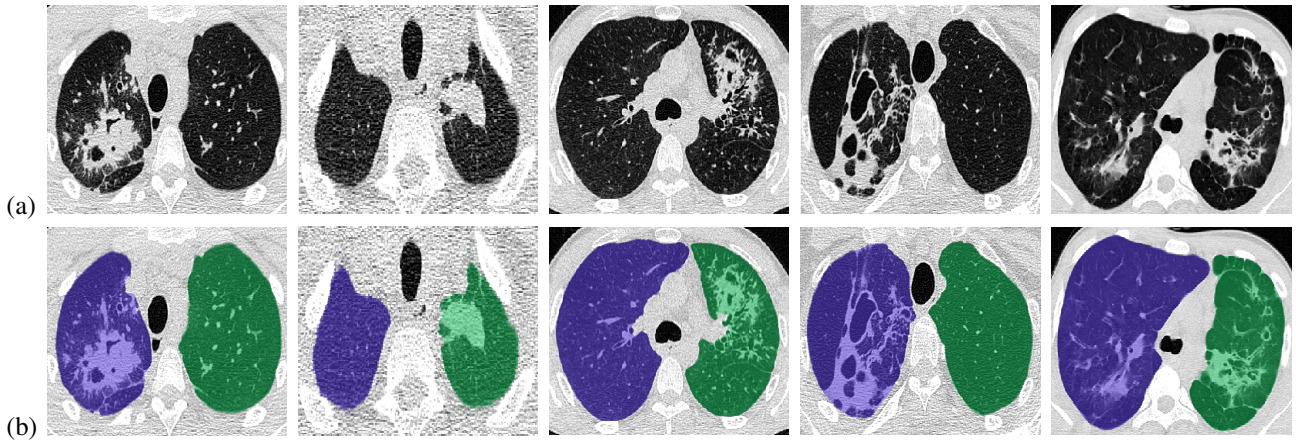


Fig. 9. Segmenting pathological lungs from the LOLA11 database: (a) original CT sections with, from left to right, fibrosis, lung mass (tumor), consolidation, cavitation + fibrosis, and fibrosis, and (b) our segmentation (its accuracy has been evaluated by the LOLA11 organizers [37]).

433 forming manual seeding mode, recommended in its video  
434 tutorial default settings for refining segmented region maps: filling  
435 holes with a 3 mm-diameter binary filter and checking fuzzy  
436 connectedness. Figure 7 compares our and FC segmentation  
437 qualitatively on a representative set of four pathological lungs  
438 from the UoLDB. The DSC, BHD, and PVD statistics for the  
439 UoLDB in Table II show that our segmentation, accounting  
440 for both short/long-range local and global lung properties, is  
441 more accurate. Differences between the metrics means for  
442 our and FC are statistically significant by the paired *t*-test  
443 (corresponding *p*-values are below 0.0001).

444 To evaluate its robustness to a chosen CT scanner and  
445 scanning protocol, our segmentation was tested against the  
446 FC framework on the VESSEL database [35] containing the  
447 CT chest images of mostly normal and a few pathological  
448 lungs. The VESSEL data sets were collected with different

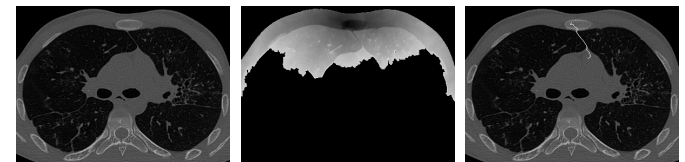


Fig. 10. Lung separation process; (a) an original slice; (b) generated energies of pixels traversed until finding the optimum path, and (c) the original image with the overlaid separating path.

449 scanners and protocols. More details can be found in [36].  
450 Figure 8 qualitatively compares both frameworks, and the  
451 DSC, BHD, and PVD statistics for segmenting the whole  
452 VESSEL database are presented in Table II. The ground truth  
453 for this database was provided by the ISBI 2012 VESSEL  
454 challenge organizers.

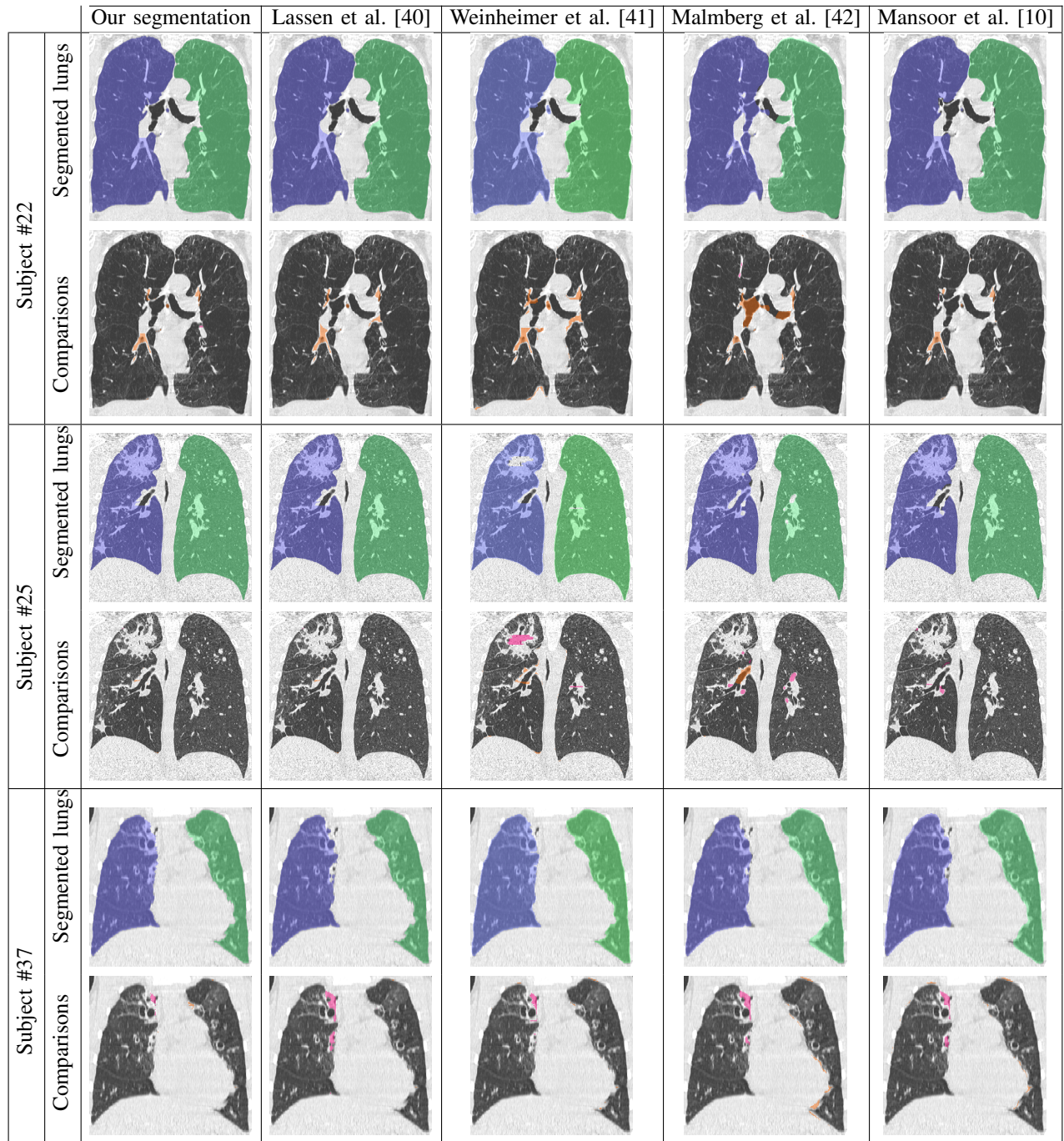


Fig. 11. Our segmentation for 3 subjects from the LOLA11 database vs. the 2<sup>nd</sup>- to 5<sup>th</sup>-rank LOLA11 competitors (the LOLA11 organizers [37] compared the extracted lungs with their ground truth and accounted for differences, being orange/pink-coded in the above region maps, to evaluate the overall accuracy).

Finally, our segmentation has been tested on the LOLA11 database [37], acquired by different scanners and protocols for 55 subjects with diverse lung pathologies. To follow the LOLA11 challenge regulations, the trachea and main bronchi have been removed from the LOLA11 image by customized region growing, which terminates after the trachea starts to split into four components. Then, if necessary, the lungs were separated with the optimal path finder [43] searching for intensity differences. The search is conducted on a 2D axial slice after finding a single connected component with a lung volume being nearly equal to the volume of the lung components

in the previous slice. The finder connects two automatically initialized points in the chest region that separates the left and right lungs, as described in [43]. Figure 10 shows an example slice together with its calculated pixel-wise energies to search for the optimum path between the two automatically initialized points and the separation path found.

The LOLA11 challenge organizers blindly compared our results, exemplified in Fig. 9, to the ground truth and reported the mean right and left lungs overlaps over all the 55 scans. Table III and Fig. 11 compare the top-rank LOLA11 methods, our results having the first rank out of the 16 competitors.

TABLE III

MEAN $\pm$ STANDARD DEVIATION OVERLAP OF OUR SEGMENTATION WITH THE GROUND TRUTH FOR THE ENTIRE LOLA11 DATABASE OF 55 CHEST CT IMAGES VS. THE 2<sup>ND</sup>–5<sup>TH</sup>-RANK LOLA11 COMPETITORS (THESE ACCURACIES WERE PROVIDED BY THE LOLA11 ORGANIZERS [37]).

Segmentation Method				
Our	[40]	[41]	[42]	[10]
0.980 $\pm$ 0.075	0.973 $\pm$ 0.116	0.970 $\pm$ 0.113	0.969 $\pm$ 0.134	0.968 $\pm$ 0.116

477

#### IV. CONCLUSIONS

478 Accurate segmentation of lung images, especially in the  
 479 case of pathological lungs with, e.g., lung nodules, is essential  
 480 for reliable CAD of pulmonary and lung diseases. Most  
 481 segmentation errors are due to missing pathological tissues;  
 482 however, these errors negligibly affect the overall segmentation  
 483 accuracy because the pathological tissue volume is often very  
 484 small compared to the whole lung volume, as in Fig. 12(A).  
 485 Nonetheless, segmentation inaccuracies of these types of tu-  
 486 mors are a serious problem, because the undetected and non-  
 487 localized tumor candidates will compromise the further anal-  
 488 ysis, e.g., detection and diagnostics, in any CAD system and  
 489 preclude the early cancer diagnosis of a patient. Even though  
 490 missing the tumor in Fig. 12(A) reduces the overall DSC by  
 491 only 0.1%, it may explain the small difference (0.7%) between  
 492 the mean overlap scores for our segmentation and the closest  
 493 competitor on the LOLA11 challenge database of pathological  
 494 lungs. Moreover, if a severe lung pathology affects a larger  
 495 portion of the total lung volume, the inaccurate segmentation  
 496 of these tissues will considerably reduce the overall accuracy,  
 497 such as in Fig. 12(B) where the overall DSC has decreased  
 498 by 30.4%. Therefore, accurate lung segmentation for various  
 499 pathologies is a must for choosing a proper region of interest  
 500 for subsequent CAD steps.

501 The methodology proposed in this paper can accurately  
 502 segment a wide range of pathological lungs from the 3D  
 503 chest CT scans due to the combining first- and second-order  
 504 probabilistic descriptors of the original and GSS-smoothed  
 505 images with the proposed appearance-guided adaptive shape  
 506 prior. The latter requires a reasonably large training set of  
 507 healthy and pathological lungs. To be accurately aligned, both  
 508 the right and left lungs in each input CT image should have  
 509 some healthy tissues to be used as guiding landmarks for  
 510 alignment. Therefore, too small healthy sections in either the  
 511 left or right lung will affect our segmentation performance, as  
 512 demonstrated in Fig. 13. To extend the scope of the proposed  
 513 segmentation technique in the future, we plan to append the  
 514 healthy tissues with other chest landmarks.

515 The high DSC, MHD, and PVD accuracy of our lung  
 516 segmentation framework has been confirmed experimentally  
 517 on multiple *in-vivo* 3D CT image datasets. What is most  
 518 importantly, the blind comparison with the publicly-available  
 519 LOLA11 database has validated the superior performance  
 520 of our framework over many existing methods in segment-  
 521 ing various pathological lung images, ranging from mild to  
 522 severe cases, such as pulmonary fibrosis, pleural effusion,  
 523 consolidation, and cavities. These wider capabilities stem from

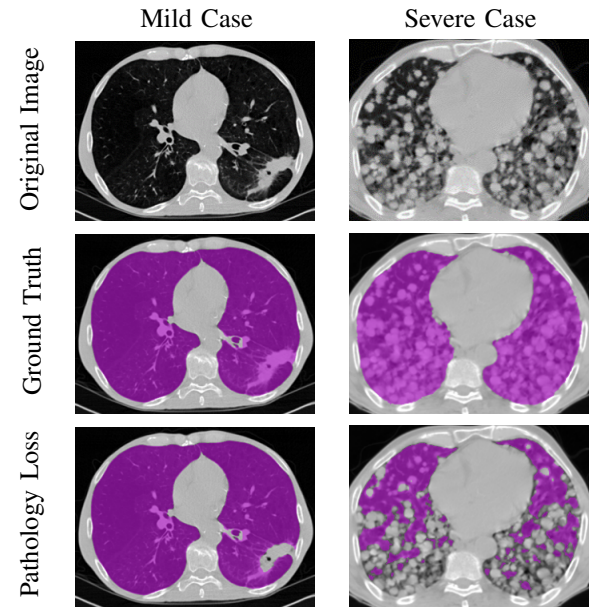


Fig. 12. Total accuracy reduction due to erroneous segmentation of pathological tissues between ground truth (b) and pathological-missing segmentation (c): only 0.1% for missing the lung mass for a tumor (first column), but about 30% for a severe pathology (second column).

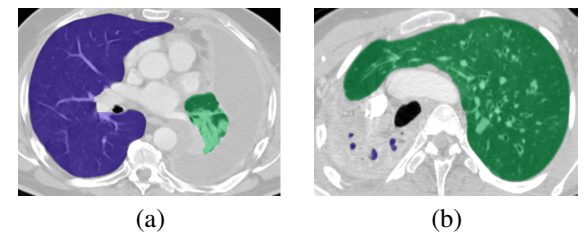


Fig. 13. Impacts of severe right and left lung pathologies on our segmentation accuracy: the ground-truth-to-left-lung overlaps of 87.4% (a) and 5.2% (b), the true lung maps being available to only the LOLA11 organizers.

524 using the adaptive prior shape model of the lungs to derive  
 525 more accurate visual appearance descriptions of the chest CT  
 526 images. The resulting higher accuracy can be beneficial for any  
 527 current CAD system that uses lung segmentation as a critical  
 528 initial step for measuring or estimating various biomarkers,  
 529 such as a whole lung volume, volumes of the left and right  
 530 lungs, and so forth [44]. These biomarkers assist in diagnosing  
 531 many restrictive / obstructive lung diseases, such as interstitial  
 532 lung disease, chronic obstructive pulmonary disease, extrinsic  
 533 disorders, and asthma. Finally, our framework can enhance  
 534 the accuracy of any lung CAD system, e.g., the one for early  
 535 detection of lung nodules because the correctly extracted lung  
 536 fields constrain and accurately identify the search space for  
 537 the nodules.

#### APPENDIX A LIST OF ALGORITHMS

**Input:** 3D-CT chest volume  $\mathbf{g}$

**Output:** GSS-smoothed volumes  $\mathbf{g}_\sigma = \mathbf{g} * \mathbf{h}_\sigma; \sigma^2 \in [4.5, 8.5]$

```

1 begin
2   forall  $\sigma^2 \in [4.5, 8.5]$  do
3     // Generate the Gaussian kernel
4      $\mathbf{h}_\sigma = \left( h_{\sigma:\rho} = \frac{1}{(2\pi)^{1.5}\sigma^3} \exp\left(-\frac{1}{2\sigma^2}(x_\rho^2 + y_\rho^2 + z_\rho^2)\right) : \rho = (x_\rho, y_\rho, z_\rho) \in \mathbf{R}_{\text{kernel}} \right)$ 
5     // Convolve the generated kernel with the input volume  $\mathbf{g}$ .
6      $\mathbf{g}_\sigma = \mathbf{g} * \mathbf{h}_\sigma = \left( g_{\sigma:r} = \sum_{\rho \in \mathbf{R}_{\text{kernel}}} h_{\sigma:\rho} \cdot g_{r-\rho} : r \in \mathbf{R} \right)$ 
7   return  $\mathbf{g}_\sigma$ 
8 end
9 end

```

**Algorithm 1:** Gaussian scale space smoothing.

Input	Output		
	$9 \times 9 \times 5$	$17 \times 17 \times 5$	$33 \times 33 \times 5$

Fig. 14. Axial planar sections of the original 3D CT image and its GSS-smoothed versions obtained with the  $9 \times 9 \times 5$ ,  $17 \times 17 \times 5$ , and  $33 \times 33 \times 5$  kernels.

**Input:** 3D-CT chest volume  $\mathbf{g}$

**Output:** Initial segmentation map  $\mathbf{m}$

```

1 begin
2   Collect the empirical gray level distribution  $\mathbf{F} = (F_q : q \in \mathbf{Q})$  for the input volume  $\mathbf{g}$ .
3   Approximate  $\mathbf{F}$  with a mixture  $\mathbf{P}_2 = w_0 \mathbf{D}_0 + w_1 \mathbf{D}_1$  of two DGs  $\mathbf{D}_k$ ;  $k \in \{0, 1\}$ ;  $w_0 + w_1 = 1$ , for two dominant
4   modes of  $\mathbf{F}$  associated with background ( $k = 0$ ) and lung ( $k = 1$ ) voxels;  $\mathbf{P}_2 = (P_{2:q} : q \in \mathbf{Q})$ .
5   Approximate deviations,  $\Delta = (F_q - P_{2:q} : q \in \mathbf{Q})$ , between  $\mathbf{F}$  and  $\mathbf{P}_2$  with sign-alternate subordinate DGs:
6     Separate positive,  $\Delta_p = (\max\{\Delta_q, 0\} : q \in \mathbf{Q})$ , and negative,  $\Delta_n = (\min\{\Delta_q, 0\} : q \in \mathbf{Q})$ , deviations.
7     Form two scaled-up “distributions”  $\mathbf{F}_p = \frac{1}{s} \Delta_p$  and  $\mathbf{F}_n = -\frac{1}{s} \Delta_p$ ;  $s = \sum_{q \in \mathbf{Q}} \Delta_{p:q} \equiv -\sum_{q \in \mathbf{Q}} \Delta_{n:q}$ .
8     Approximate  $\mathbf{F}_p$  and  $\mathbf{F}_n$  with subordinate DG mixtures of estimated sizes  $C_p$  and  $C_n$ , respectively:
9        $\mathbf{P}_{p:C_p} = s \sum_{k=1}^{C_p} w_{p:k} \mathbf{D}_{n:k}$  and  $\mathbf{P}_{n:C_n} = s \sum_{l=1}^{C_n} w_{n:l} \mathbf{D}_{n:l}$ .
10      Add the scaled-down subordinate LCDG  $s(\mathbf{P}_{p:C_p} - \mathbf{P}_{n:C_n})$  to the mixture  $\mathbf{P}_2$  to get the initial LCDG:
11         $\mathbf{P}_C = w_0 \mathbf{D}_0 + w_1 \mathbf{D}_1 + s \sum_{k=1}^{C_p} w_{p:k} \mathbf{D}_{n:k} - s \sum_{l=1}^{C_n} w_{n:l} \mathbf{D}_{n:l}$  of size  $C = 2 + C_p + C_n$ .
12        // The initial LCDG has 2 positive weights  $w_0$  and  $w_1$  of the dominant DGs and  $C_p + C_n$  weights
13        // of the subordinate sign alternate DGs, such that  $\sum_{k=1}^{C_p} w_{p:k} - \sum_{l=1}^{C_n} w_{n:l} = 0$ .
14      Allocate the subordinate DGs to the lung or background dominant DG to minimize overlaps between the final
15      separate lung and background LCDG models.
16 end

```

**Algorithm 2:** 1<sup>st</sup>-order intensity modeling with linear combinations of discrete Gaussians (LCDG)

Original Image		GSS smoothing	
Input	Output	Input	Output

Fig. 15. Initial segmentation maps after voxel-wise classification by the LCDG modeling of original and GSS-smoothed images.

**Input:** Initial segmentation 3D map  $\mathbf{m}$ ; numbers of neighbors  $c_{\text{hvdc}} = 8$ ,  $c_{\text{hvdu}} = c_{\text{hvdl}} = 9$ .

**Output:** 4D array  $\mathbf{P} = (P_r[k] : r \in \mathbf{R}; k \in \{0, 1\})$ .

```

1 begin
2   Read the initial 3D map  $\mathbf{m}$ 
3   // Calculate Gibbs potentials  $V_{a:\text{eq}}$  and  $V_{a:\text{ne}}$ ;  $a \in \{\text{hvdc}, \text{hvdu}, \text{hvdl}\}$  of Eq. (6) for the map  $\mathbf{m}$  by collecting
4   // frequencies  $f_{\text{eq}:a}(\mathbf{m})$  and  $f_{\text{ne}:a}(\mathbf{m}) = 1 - f_{\text{eq}:a}(\mathbf{m})$  of equal and non-equal neighboring pairs of region labels.
5   foreach neighborhood  $a \in \{\text{hvdc}, \text{hvdu}, \text{hvdl}\}$  do
6     |  $N_{\text{eq}:a} \leftarrow 0$ ;  $N_a \leftarrow 0$ 
7   end
8   foreach voxel  $r \in \mathbf{R}$  do
9     | foreach neighborhood  $a \in \{\text{hvdc}, \text{hvdu}, \text{hvdl}\}$  do
10    |   | // Find the number  $\nu_{\text{eq}:a}$  of labels in the neighborhood  $a$ , which are equal to the label  $m_r$ 
11    |   |  $N_{\text{eq}:a} \leftarrow N_{\text{eq}:a} + \nu_{\text{eq}:a}$ ;  $N_a \leftarrow N_a + c_a$ 
12    |   end
13  end
14  // Calculate frequencies  $f_{\text{eq}:a}$  and negated potentials  $V_{\text{eq}:a}$  of equal labels.
15  foreach neighborhood  $a \in \{\text{hvdc}, \text{hvdu}, \text{hvdl}\}$  do
16    |  $f_{\text{eq}:a} \leftarrow \frac{N_{\text{eq}:a}}{N_a}$ ;  $V_{\text{eq}:a} \leftarrow 4f_{\text{eq}:a} - 2$ ;  $V_{\text{ne}:a} = -V_{\text{eq}:a}$ 
17  end
18  // Compute transitional probabilities  $\mathbf{P}$  using voxel-wise Gibbs neg-energies  $E[k]$ 
19  foreach voxel  $r \in \mathbf{R}$  do
20    | foreach label  $k$  do
21      |   | // Compute the voxel-wise neg-energies  $E_0$  and  $E_1$ .
22      |   |  $E_k \leftarrow 0$ 
23      |   | foreach neighborhood  $a \in \{\text{hvdc}, \text{hvdu}, \text{hvdl}\}$  do
24        |   |   | // Find the number  $\nu_{\text{eq}:a:k}$  of neighboring voxel labels equal to  $k$ .
25        |   |   |  $E_k \leftarrow E_k + \nu_{\text{eq}:a:k} \cdot V_{\text{eq}:a} + (c_a - \nu_{\text{eq}:a:k}) \cdot V_{\text{ne}:a}$ 
26      |   | end
27    | end
28    | foreach label  $k$  do
29      |   |  $P_r[k] = \frac{\exp(E_k)}{\exp(E_0) + \exp(E_1)}$ 
30    | end
31  end
32 return  $\mathbf{P}$ 
33 end

```

**Algorithm 3:** Learning the MGRF model of the input map.

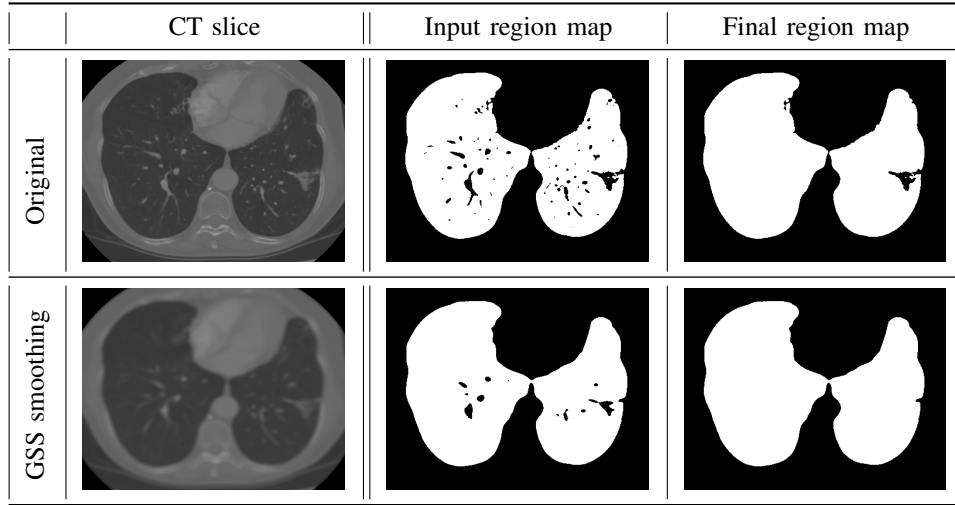


Fig. 16. MGRF-guided segmentation of original image and its GSS smoothed version.

**Input:** Test image  $t$ ; co-aligned training database  $B = \{g_i : i = 1, \dots, N\}$ .

**Output:** 4D shape prior  $P_{sh} = (P_{sh:r} : r \in R)$

```

1 begin
2   // Align t to B and store the deformation field  $\psi$  that maps each test voxel to the database domain
3   // Select top J database images by normalized cross correlation (NCC) with the co-aligned test image
4   foreach image  $g_i \in B$  do
5      $NCC_{t,g_i} = \frac{\sum_{r \in R} (t_r - \mu_t)(g_{i:r} - \mu_{g_i})}{\sqrt{\sum_{r \in R} (t_r - \mu_t)^2} \sqrt{\sum_{r \in R} (g_{i:r} - \mu_{g_i})^2}}$ 
6   end
7   // Form the atlas  $B_A$  from J closest, by the NCC, training images.
8   foreach voxel  $r \in R$  do
9     // Map the voxel  $r$  to the atlas  $B_A$  using the deformation field  $\psi$ .
10    while matches between the signal  $t_r$  and the atlas signals are not found do
11      // Initialize the matching tolerance:  $\tau \leftarrow \tau_{init}$ 
12      // Loop until  $\tau$  reaches a predefined threshold  $\xi$ 
13      while  $\tau < \xi$  do
14        // Find within the search cube  $C_{r:\alpha}$  a subset of all matching voxels  $\nu_r = \bigcup_{j=1}^J \nu_{j:r}$  where
15         $\nu_{j:r} = \{\rho : \rho \in C_r; |t_r - g_{j:\rho}| \leq \tau\}$  is the matching subset in the atlas image  $g_j \in B_A$ .
16        if matching voxels are found in  $C_r$  then
17          // Compute the voxel-wise region label probability  $P_{sh:r}(k); k \in \{0, 1\}$ , using the training labels
18          // and the numbers of voxels  $\nu_{j:r}$  in the subsets  $\nu_{j:r}$ .
19           $\nu_r \leftarrow \sum_{j=1}^J \nu_{j:r}$ 
20           $P_{sh:r}(k) \leftarrow \frac{1}{\nu_r} \sum_{j=1}^J \sum_{\rho \in \nu_{j:r}} \delta(k - m_{j:\rho}); k \in \{0, 1\}$ 
21          // where  $\delta(w)$  is the Kronecker's delta-function:  $\delta(0) = 1$  and  $\delta(w) = 0$  for  $w \neq 0$ .
22          break
23        else
24          // increment the matching threshold
25           $\tau \leftarrow \tau + \Delta_\tau$ 
26        end
27      end
28    end
29    // increment the search cube size
30     $\alpha \leftarrow \alpha + \Delta_{size}$ 
31  end
32 end
33 return  $P_{sh}$ 
34 end

```

**Algorithm 4:** Adaptive shape prior

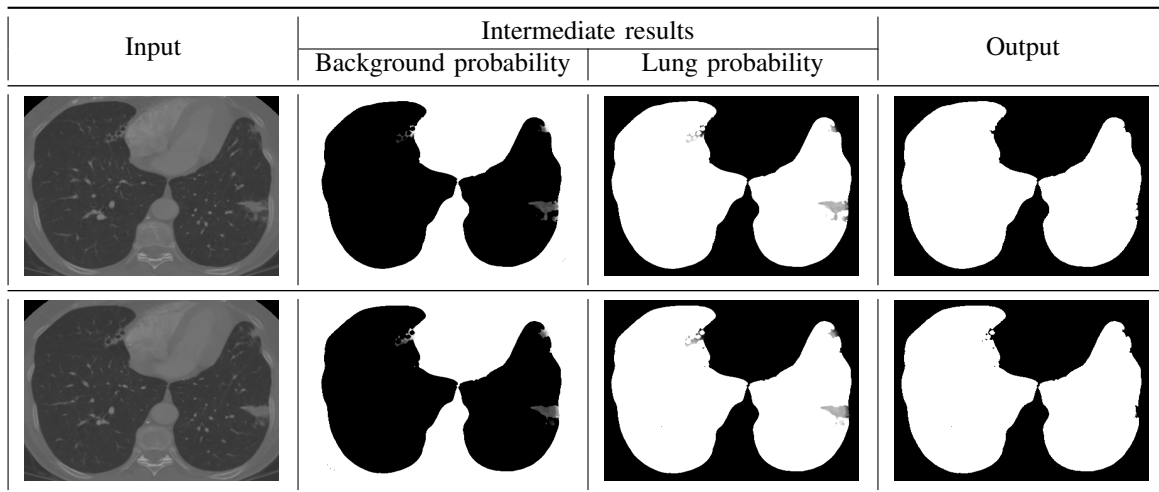


Fig. 17. Axial planar sections of the 3D CT images; background / lung shape probabilities, and the final segmentation maps.

542

## REFERENCES

- 543 [1] A. Cunliffe, S. G. Armato, R. Castillo, N. Pham, T. Guerrero, and H. A. Al-Hallaq, "Lung texture in serial thoracic computed tomography scans: Correlation of radiomics-based features with radiation therapy dose and radiation pneumonitis development," *Int. J. Rad. Oncol.\* Biol.\* Phys.*, vol. 91, no. 5, pp. 1048–1056, 2015.
- 544 [2] S. G. Armato and W. F. Sensakovic, "Automated lung segmentation for thoracic ct: Impact on computer-aided diagnosis1," *Aca. Radiol.*, vol. 11, no. 9, pp. 1011–1021, 2004.
- 545 [3] S. Hu, E. Hoffman, and J. Reinhardt, "Automatic lung segmentation for accurate quantitation of volumetric X-ray CT images," *IEEE Trans. Med. Imaging*, vol. 20, pp. 490–498, 2001.
- 546 [4] A. M. Mendonça, J. A. da Silva, and A. Campilho, "Automatic delimitation of lung fields on chest radiographs," in *Proc. IEEE Int. Symp. Biomed. Imaging*, vol. 2, 2004, pp. 1287–1290.
- 547 [5] P. Campadelli, E. Casiraghi, and D. Artioli, "A fully automated method for lung nodule detection from postero-anterior chest radiographs," *IEEE Trans. Med. Imaging*, vol. 25, no. 12, pp. 1588–1603, 2006.
- 548 [6] B. van Ginneken, M. B. Stegmann, and M. Loog, "Segmentation of anatomical structures in chest radiographs using supervised methods: A comparative study on a public database," *Med. Image Anal.*, vol. 10, pp. 19–40, 2006.
- 549 [7] P. Korfiatis, S. Skiadopoulos, P. Sakellaropoulos, C. Kalogeropoulou, and L. Costaridou, "Combining 2D wavelet edge highlighting and 3D thresholding for lung segmentation in thin-slice CT," *Br. J. Radiol.*, vol. 80, no. 960, pp. 996–1004, 2007.
- 550 [8] M. Silveira, J. Nascimento, and J. Marques, "Automatic segmentation of the lungs using robust level sets," in *Proc. IEEE Int. Conf. Eng. Med. Biol.*, 2007, pp. 4414–4417.
- 551 [9] J. C. Ross, R. S. J. Estépar, A. Díaz, C.-F. Westin, R. Kikinis, E. K. Silverman, and G. R. Washko, "Lung extraction, lobe segmentation and hierarchical region assessment for quantitative analysis on high resolution computed tomography images," in *Med. Image Comput. Comput.-Ass. Interven.*, vol. 5762, 2009, pp. 690–698.
- 552 [10] A. Mansoor, U. Bagci, Z. Xu, B. Foster, K. N. Olivier, J. M. Elinoff, A. F. Suffredini, J. K. Udupa, and D. J. Mollura, "A generic approach to pathological lung segmentation," *IEEE Trans. Med. Imaging*, vol. 33, no. 12, pp. 2293–32 210, 2014.
- 553 [11] J. Wang, F. Li, and Q. Li, "Automated segmentation of lungs with severe interstitial lung disease in CT," *Med. Phys.*, vol. 36, no. 10, pp. 4592–4599, 2009.
- 554 [12] T. T. Kockelkorn, C. M. Schaefer-Prokop, G. Bozovic, A. Muñoz-Barrutia, E. M. van Rikxoort, M. S. Brown, P. A. de Jong, M. A. Viergever, and B. van Ginneken, "Interactive lung segmentation in abnormal human and animal chest CT scans," *Med. Phys.*, vol. 41, no. 8, p. 081915, 2014.
- 555 [13] J. Zhou, B. Zhang, G. Lasio, K. Prado, and W. D'Souza, "SU-F-BRF-02: Automated lung segmentation method using atlas-based sparse shape composition with a shape constrained deformable model," *Med. Phys.*, vol. 41, no. 6, pp. 399–399, 2014.
- 556 [14] I. Sluimer, M. Prokop, and B. Van Ginneken, "Toward automated segmentation of the pathological lung in CT," *IEEE Trans. Med. Imaging*, vol. 24, no. 8, pp. 1025–1038, 2005.
- 557 [15] S. Sun, C. Bauer, and R. Beichel, "Automated 3-D segmentation of lungs with lung cancer in CT data using a novel robust active shape model approach," *IEEE Trans. Med. Imaging*, vol. 31, no. 2, pp. 449–460, 2012.
- 558 [16] E. M. van Rikxoort, B. de Hoop, M. A. Viergever, M. Prokop, and B. van Ginneken, "Automatic lung segmentation from thoracic computed tomography scans using a hybrid approach with error detection," *Med. Phys.*, vol. 36, pp. 2934–2947, 2009.
- 559 [17] K. Nakagomi, A. Shimizu, H. Kobatake, M. Yakami, K. Fujimoto, and K. Togashi, "Multi-shape graph cuts with neighbor prior constraints and its application to lung segmentation from a chest CT volume," *Med. Image Anal.*, vol. 17, pp. 62–77, 2013.
- 560 [18] P. Korfiatis, C. Kalogeropoulou, A. Karahaliou, A. Kazantzi, S. Skiadopoulos, and L. Costaridou, "Texture classification-based segmentation of lung affected by interstitial pneumonia in high-resolution CT," *Med. Phys.*, vol. 35, no. 12, pp. 5290–5302, 2008.
- 561 [19] B. Lassen, J.-M. Kuhnigk, O. Friman, S. Krass, and H.-O. Peitgen, "Automatic segmentation of lung lobes in CT images based on fissures, vessels and bronchi," in *Proc. IEEE Int. Symp. Biomed. Imaging*, 2010, pp. 560–563.
- 562 [20] N. Birkbeck, T. Kohlberger, J. Zhang, M. Sofka, J. Kaftan, D. Comanicu, and S. K. Zhou, "Lung segmentation from CT with severe pathologies using anatomical constraints," *Med. Image Comput. Comput.-Ass. Interven.*, vol. 8673, no. 1, pp. 804–811, 2014.
- 563 [21] T. Kockelkorn, E. M. van Rikxoort, J. C. Grutters, and B. van Ginneken, "Interactive lung segmentation in CT scans with severe abnormalities," in *Proc. IEEE Int. Symp. Biomed. Imaging*, 2010, pp. 564–567.
- 564 [22] P. Hua, Q. Song, M. Sonka, E. A. Hoffman, and J. M. Reinhardt, "Segmentation of pathological and diseased lung tissue in CT images using a graph-search algorithm," in *Proc. IEEE Int. Symp. Biomed. Imaging*, 2011.
- 565 [23] A. El-Baz, G. M. Beach, G. Gimel'farb, K. Suzuki, K. Okada, A. Elnakib, A. Soliman, and B. Abdollahi, "Computer-aided diagnosis systems for lung cancer: challenges and methodologies," *International Journal of Biomedical Imaging*, vol. 2013, 2013.
- 566 [24] K. Li, X. Wu, D. Z. Chen, and M. Sonka, "Optimal surface segmentation in volumetric images—A graph-theoretic approach," *IEEE Trans. Pattern Anal. Mach. Intell.*, vol. 28, no. 1, pp. 119–134, 2006.
- 567 [25] M. Sofka, J. Wetzel, N. Birkbeck, J. Zhang, T. Kohlberger, J. Kaftana, J. Declerck, and S. K. Zhou, "Multi-stage learning for robust lung segmentation in challenging CT volumes," in *Med. Image Comput. Comput.-Ass. Interven.*, 2011, pp. 667–674.
- 568 [26] J. K. Udupa and S. Samarasekera, "Fuzzy connectedness and object definition: Theory, algorithms and applications in image segmentation," *Graph. Models and Image Process.*, vol. 58, no. 3, pp. 246–261, 1996.
- 569 [27] B. Glocker, A. Sotiras, N. Komodakis, and N. Paragios, "Deformable medical image registration: Setting the state of the art with discrete methods," *Ann. Rev. Biomed. Eng.*, vol. 13, pp. 219–244, 2011.
- 570 [28] T. Lindeberg, "Generalized Gaussian scale-space axiomatics comprising

- 643 linear scale-space, affine scale-space and spatio-temporal scale-space,"  
644 *J. Mathem. Imag. Vis.*, vol. 40, no. 1, pp. 36–81, 2011.  
645 [29] A. Farag, A. El-Baz, and G. Gimel'farb, "Precise segmentation of multi-  
646 modal images," *IEEE Trans. Image Process.*, vol. 15, no. 4, pp. 952–968,  
647 2006.  
648 [30] G. L. Gimel'farb, *Image Textures and Gibbs Random Fields*. Kluwer  
649 Academic, 1999.  
650 [31] B. Glocker, N. Komodakis, G. Tziritas, N. Navab, and N. Paragios,  
651 "Dense image registration through MRFs and efficient linear program-  
652 ming," *Medical Image Analysis*, vol. 12, no. 6, pp. 731–741, 2008.  
653 [32] B. Glocker, N. Komodakis, N. Paragios, and N. Navab, "Non-rigid  
654 registration using discrete MRFs: Application to thoracic CT images,"  
655 in *Medical Image Analysis for the Clinic – A Grand Challenge*, 2010,  
656 pp. 147–154.  
657 [33] Y. Lu, I. Cohen, X. S. Zhou, and Q. Tian, "Feature selection using  
658 principal feature analysis," in *Proceedings of the 15th ACM international  
659 conference on Multimedia*. ACM, 2007, pp. 301–304.  
660 [34] A. El-Baz, A. Elnakib, F. Khalifa, M. A. El-Ghar, P. McClure, A. Soli-  
661 man, and G. Gimel'farb, "Precise segmentation of 3-D magnetic res-  
662 onance angiography," *IEEE Trans. Biomed. Eng.*, vol. 59, no. 7, pp.  
663 2019–2029, 2012.  
664 [35] "VESSEL SEgmentation in the Lung 2012," [http://vessel12.  
665 grand-challenge.org/](http://vessel12.grand-challenge.org/), 2012.  
666 [36] R. D. Rudyanto, S. Kerkstra, E. M. Van Rikxoort, C. Fetita, P.-Y. Brillet,  
667 C. Lefevre, W. Xue, X. Zhu, J. Liang, İ. Öksüz *et al.*, "Comparing  
668 algorithms for automated vessel segmentation in computed tomography  
669 scans of the lung: the VESSEL12 study," *Med. Image Anal.*, vol. 18,  
670 no. 7, pp. 1217–1232, 2014.  
671 [37] "LOBe and Lung Analysis 2011," <http://lola11.com/>, 2011.  
672 [38] K. H. Zou, S. K. Warfield, A. Bharatha, C. M. C. Tempany, M. R. Kaus,  
673 S. J. Haker, W. M. Wells III, F. A. Jolesz, and R. Kikinis, "Statistical  
674 validation of image segmentation quality based on a spatial overlap  
675 index," *Aca. Radiol.*, vol. 11, no. 2, pp. 178–189, 2004.  
676 [39] G. Gerig, M. Jomier, and M. Chakos, "Valmet: A new validation tool  
677 for assessing and improving 3D object segmentation," in *Med. Image  
678 Comput. Comput.-Ass. Interven.*, Utrecht, The Netherlands, October 14–  
679 17, 2001, pp. 516–523.  
680 [40] B. Lassen, E. M. van Rikxoort, M. Schmidt, S. Kerkstra, B. van Gin-  
681 neken, and J.-M. Kuhnlk, "Automatic segmentation of the pulmonary  
682 lobes from chest CT scans based on fissures, vessels and bronchi," *IEEE  
683 Trans. Med. Imaging*, vol. 32, no. 2, pp. 210–222, 2013.  
684 [41] O. Weinheimer, T. Achenbach, C. P. Heussel, and C. Düber, "Auto-  
685 matic lung segmentation in mdct images," in *Proc. 4th Int. Workshop  
686 Pulmonary Image Anal. Toronto*, 2011, pp. 241–255.  
687 [42] F. Malmberg, R. Nordenskjöld, R. Strand, and J. Kullberg, "Smartpaint:  
688 A tool for interactive segmentation of medical volume images," *Comput.  
689 Methods Biomed. Biomed. Eng.: Imaging & Visual.*, pp. 1–9, 2014.  
690 [43] M. S. Brown, M. F. Mcnitt-Gray, N. J. Mankovich, J. G. Goldin, J. Hiller,  
691 L. S. Wilson, and D. Aberle, "Method for segmenting chest CT image  
692 data using an anatomical model: preliminary results," *IEEE Trans. Med.  
693 Imaging*, vol. 16, no. 6, pp. 828–839, 1997.  
694 [44] A. Fernandez-Bustamante, J. Klawitter, J. E. Repine, A. Agazio, A. J.  
695 Janocha, C. Shah, M. Moss, I. S. Douglas, Z. V. Tran, S. C. Erzurum,  
696 U. Christians, and T. Seres, "Early effect of tidal volume on lung injury  
697 biomarkers in surgical patients with healthy lungs," *Anesthesiology*, vol.  
698 121, no. 3, pp. 469–481, 2014.